AN OUT-OF-PLANE WIDE BANDWIDTH MICRO-G FM ACCELEROMETER WITH DIFFERENTIAL OUTPUT

Seungyong Shin[1], Tanya Chauhan[1], Justin Matthews[1], Haoran Wen[2] and Farrokh Ayazi[1,2]
[1]Georgia Institute of Technology, USA
and [2]StethX Microsystems, USA

ABSTRACT

This paper reports on the design, fabrication, and characterization of a vacuum encapsulated wide bandwidth micro-g out-of-plane accelerometer with differential output utilizing electrostatic frequency modulation. The accelerometer consists of a proof-mass suspended by torsional springs, differential pair of free-free beam (FFB) resonators as transducers, and top-layer polysilicon capacitive electrodes deposited and bridged over TEOS-filled trenches which define the resonators and proof-mass in the device layer of an SOI wafer. The fabricated device measures a scale factor of 41.2Hz/g with a resonator Q of 1800 and a proof-mass Q of 6.7 at 19kHz, which enable low-noise operation in a wide bandwidth. The accelerometer demonstrates high performance with a VRW corresponding to noise density of 5.8μg/√Hz and a bias instability of 23μg, without temperature compensation. The demonstrated performance, while promising, can be further improved by applying temperature compensation techniques to the electronics interface.

KEYWORDS

MEMS, frequency modulation, eFM, accelerometer

INTRODUCTION

The evolution of sensor technology has enabled a large variety of applications that improve the quality of people's daily life. For example, a high-resolution wide-bandwidth Out-of-Plane Accelerometer (OPA) can enable interesting applications such as non-invasive real-time monitoring of mechano-acoustic signals emanating from the heart and lungs, which contain important information about the health of cardiopulmonary system [1].

In order to detect subtle pulmonary signals on the skin, the accelerometer need to have very low noise (<10μg/√Hz) and a wide operational bandwidth (>10kHz). However, for conventional quasi-static capacitive MEMS accelerometers, implementation of these requirements is nontrivial due to design trade-off between noise and bandwidth. In order to overcome this trade-off, large-area submicron-gap out-of-plane capacitive electrodes are needed, which could bring additional challenges in micro-fabrication, such as stiction.

These challenges can be overcome using an electrostatic frequency modulated (eFM) accelerometer, which utilizes smaller electrodes and stiffer structures. Recently, eFM in-plane accelerometers (IPA) with differential readout have shown great potential to meet both bandwidth and noise performance while providing a good linearity and temperature stability [2]. The differential frequency readout scheme provides several important benefits. First, it effectively reduces unwanted frequency shift due to temperature variation. The identical resonators have similar TCFs, and the frequency fluctuation due to temperature variation can be canceled with differential measurement. Second, it suppresses the first order nonlinear effects in gap-closing stiffness modulation mechanism. Furthermore, frequency modulation induced by accelerations orthogonal to the sensing axis mainly results common mode response. Therefore, the differential readout remains unchanged and cross-axis sensitivity can be minimized.

Conventionally, implementation of a differential readout scheme for frequency output OPA utilizing mechanical frequency modulation is difficult due to the 2D nature of common micro-fabrication techniques [3]. However, for eFM OPA using capacitive transduction, differential readout can be achieved in a similar fashion as quasi-static capacitive OPAs [4]. At the same time, the scale factor of eFM OPA has 4th order dependency on the gap size, reducing the transduction area requirement and having significantly lower risks of stiction and pull-in instability than quasi-static capacitive OPAs [5].

Another important specification that needs to be carefully examined is the sensor response time, which is closely related to the system bandwidth. Since the operational bandwidth becomes smaller if the 2nd order proof-mass system is not near critically damped region, it is very important to have a proper damping mechanism for the proof-mass. Resonant accelerometers require high Q resonators to achieve low phase noise; therefore, vacuum packaging is imperative to minimize squeeze film air damping, which can cause the proof-mass to be under-damped and limit the sensor bandwidth [6]. By utilizing submicron gaps [7], this trade-off can be overcome by incorporating dedicated damping electrodes, enabling near-critically-damped proof-mass while maintaining a high resonator Q in vacuum encapsulation.

In this paper, the design, implementation, and characterization of a novel micro-g eFM OPA with differential output and wide open-loop bandwidth (>10kHz) are introduced and its unique design and fabrication process features are described.

OUT OF PLANE ACCELEROMETER DESIGN

The schematic of the eFM OPA is shown in Figure 1, where the device consists of an off-centered proof-mass suspended by torsional spring, two identical free-free beam (FFB) resonators, and top-layer polysilicon capacitive electrodes deposited and bridged over TEOS-filled trenches which define the resonators and proof-mass in the device layer of SOI wafer.

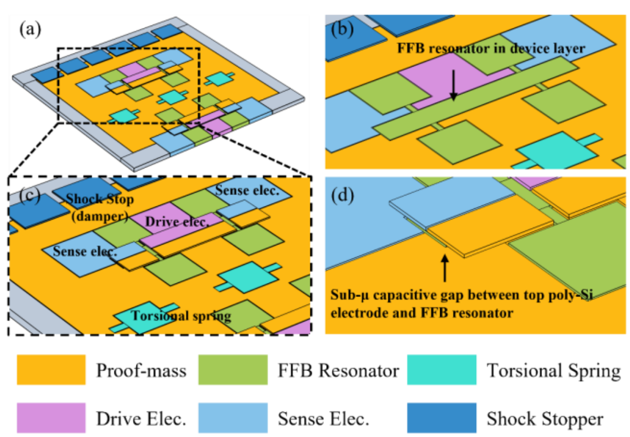

Figure 1: (a) Schematic of the differential readout eFM OPA (b) free-free beam resonator in device layer of SOI wafer which are driven, sensed, and modulated with sub-micron out-of-plane transduction gap (c) zoomed in view of the eFM accelerometer (d) zoomed-in view showing sub-micron out-of-plane gaps and poly-silicon top electrodes.

Each resonator is designed to be frequency modulated by electrostatic force (spring softening) resulting from a 200nm capacitive gap between the body of the resonator and movable polysilicon electrodes attached to the proof-mass.

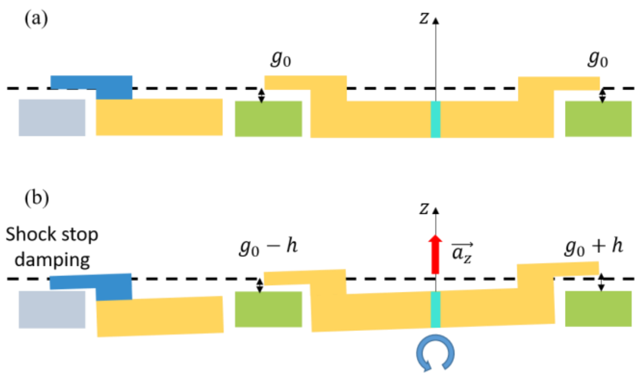

Figure 2: (a) Cross sectional view of the accelerometer. Without external acceleration, two transduction gaps remain unchanged. (b) Tilting motion due to acceleration causes a differential gap change, yielding differential frequency modulation.

As shown in Figure 2, the imbalanced proof-mass creates torque and tilting motion when external acceleration is applied. The generated torque can be expressed as equation 4.1.

$$\tau = M\vec{a} \times \vec{r} = K_\theta \times \theta \quad (1)$$

where *M* represents effective mass of the proof-mass with respect to the tilting motion, $\vec{r}$ is a vector of center-of-mass from the origin. Since the rotational angle will be very small compared to the dimensions, equivalent z-axis displacement *h* can be approximated as $d \times tan\theta \approx d\theta$, where d is distance between the anchor to the out-of-plane gap. Such a tilting motion generates differential changes of capacitive gap size as shown in Figure 2(b). When a DC voltage of V_p is applied between the proof-mass and the resonators, the change in the gap results in a change in the electrostatic force and hence the amount of spring softening for each resonator. The differential frequency output of the device is given by:

$$\Delta f_{res} = 2\frac{f_0}{\omega_{proof}^2}\frac{3}{2}\frac{\varepsilon tl}{K_{res}g_0^4}V_p^2 \times \vec{a}_{ext} \quad (2)$$

where f_0 is the unbiased resonant frequency, ω_{proof} is natural frequency of the tilting mode of the proof-mass, and K_{res} represents effective vibrational mode stiffness of the resonator (FFB mode), ε is the permittivity of air, *t* is thickness of the device, *l* is length of the transduction area, k_{res} is stiffness of the resonator, g_0 is initial gap size, and V_p is potential difference between the proof-mass and resonator. As shown in equation (2), the scale factor depends inversely on the fourth power of the transduction gap. Therefore, having smaller gap size greatly improves the sensitivity of the eFM accelerometer. For this OPA accelerometer, 200nm of transduction gap, g_0 is implemented using a process similar to the one presented in [7].

Since the nano-scale transduction gap is determined by the thickness of thermally grown sacrificial layer, there is only one capacitive gap size available through the wafer, which makes it difficult for an accelerometer leveraging translational motion of the proof mass to implement shock stop to prevent proof-mass pull-in or mechanical failure under high shock. By leveraging the off-centered teeter-totter structure shown in Figure 2, shock stop can be implemented naturally. Since the longer edge of the proof-mass has always maximum displacement under the tilting motion, the shock stop implemented at the longer side of the proof-mass hits the fixed blocking structure in device layer first under the large external acceleration. Figure 3 shows the designed shock stop structure. It has six stoper structure attached to the fixed outer frame and proof mass alternative manner, which provide shock stopping mechanism for both upward and downward direction.

Additionally, the thin out-of-plane gaps of the shock stopper structure also provide a scalable damping mechanism. With the sub-micron gap, the squeeze film air loss expressed in equation (3) can be engineered to maintain the proof-mass within near critically damped region even in vacuum environment.

$$D_{SFD} = N_e \eta_{eff} l_e \left(\frac{h_e}{g_0}\right)^3 \quad (3)$$

In this equation, N_e stands for number of electrodes, η_{eff} is viscosity of the ambient gas, l_e is electrode length, and h_e is electrode thickness, respectively. The implemented structures are shown in Figure 3. The shock stop structures are attached to the fixed frame and proof-mass alternatively which provide shock stop mechanism in both upward and downward direction which having enough amount of squeezed film air damping.

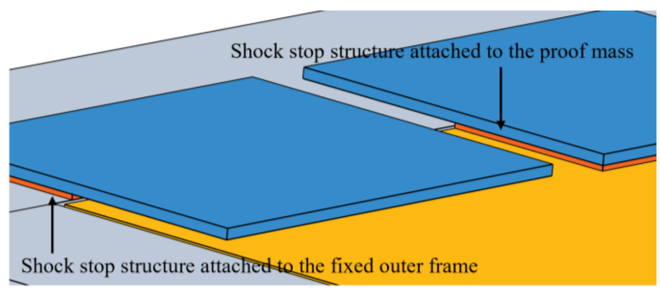

Figure 3: (Exaggerated) Schematic of shock stop structure attached to the fixed outer frame and proof mass alternatively provide shock stops for both upward and downward directions and adequate squeeze film air damping to prevent underdamped response.

The simulated resonant characteristics of the designed proof-mass show unbiased resonant frequency at 21.8kHz with quality factor of 2 corresponding to the squeezed film damping at 10Torr, which means the proof-mass can have near critical damping operation and maintain fast settling time and large operational bandwidth (Fig. 4, 5).

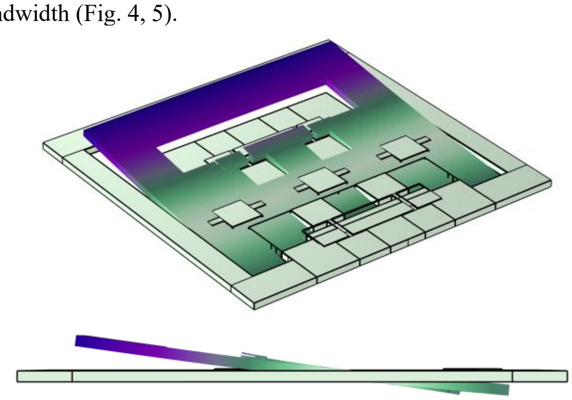

Figure 4: Resonant mode of the proof-mass @ 21.8kHz.

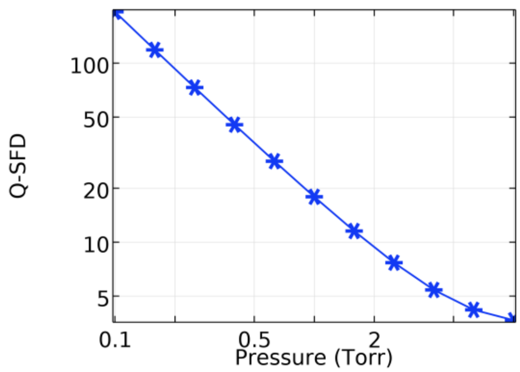

Figure 5: Simulated quality factor corresponding to the squeezed film air damping shows Q of 2 @ 10Torr.

The FFB resonators at 650kHz have low flexure mode stiffness and provides large active transduction area, which enables higher scale factor while having high translational mode stiffness to prevent pull-in instability (Fig. 6).

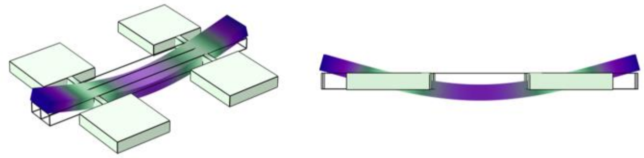

Figure 6: Free-free beam resonator showing un-biased resonant frequency of 650kHz

Moreover, it is possible to design tether and anchor structures in a manner to minimize mechanical coupling loss through the substrate (Q_{ANCHOR}>>1M). The simulated resonator Q due to various mechanisms are summarized in Table 1. Additionally, 200 nm out of plane transduction gap also provide very low motional impedance. The simulation result shows motional impedance of 30.5kΩ for the FFB resonators.

Table 1: Simulated quality factor contributions of the free-free beam resonator.

Resonator Q contribution	
Q_{ANCHOR}	6.2M
Q_{TED}	65.3k
Q_{SFD}@1torr	12.5k
Q_{SFD}@10torr	1.8k

Since the body of the two resonators are electrically isolated from one another, slightly different DC bias voltages can be applied to resonators to provide a second order compensation of the device over temperature in the presence of fabrication imperfections. The differential configuration provides significant benefits by canceling unwanted common mode uncertainties such as temperature coefficient of frequency of the resonators, and the first order nonlinearity in gap-closing frequency modulation. The simulated scale factor nonlinearity is less than 0.5% over ±10g.

EXPERIMENTAL RESULTS

The devices are fabricated on an SOI wafer with 40μm thick device layer and hermetically sealed by Si-Au eutectic wafer bonding targeting 5~10 Torr vacuum level without using a getter. Figure 7 shows colored SEM of a fabricated (un-capped) device.

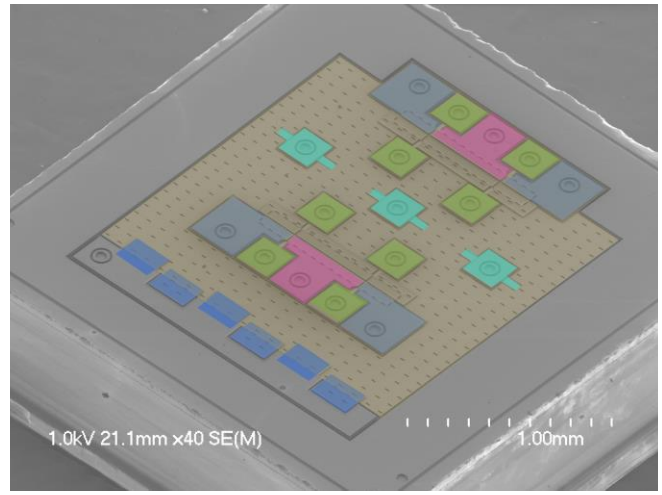

Figure 7: SEM image of a fabricated eFM OPA. The device footprint is 2mm×2mm. (color coding is same as Figure 1)

The fabricated device was interfaced with TIA and measured using vector network analyzer. Figure 8 shows a typical resonant characteristic of a pair of FFB resonators (Q of ~1800 @ 626kHz) with statistical data revealing average resonator Q of 2200 across several capped devices.

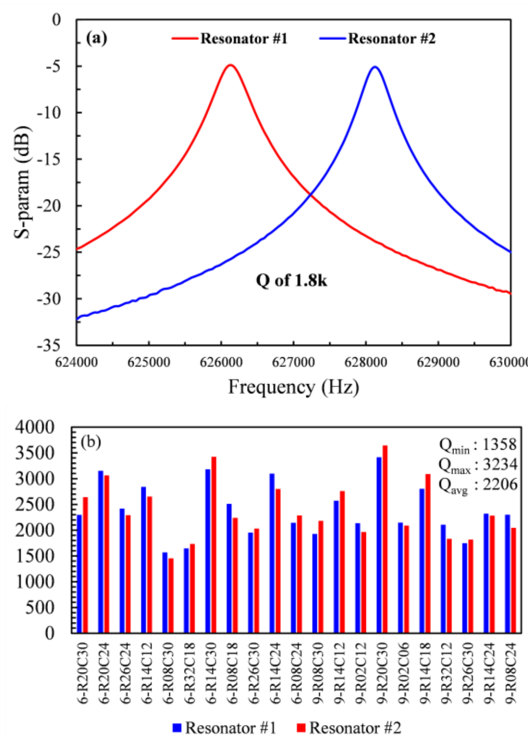

Figure 8: Typical resonant characteristics of proof-mass (a) and differential pair of resonators (b) Statistics of the FFB resonator Q across dies show average Q of ~2,200.

Figure 9 shows measured near critically damped resonant characteristics of the proof-mass (Q of 6.7 @ 19.1kHz). The proof-mass quality factor of 6.3 indicates that system rising time of 18μs and settling time of 0.5ms. A multi-order digital low-pass filter can be applied at the post processing stage to obtain even faster sensor response time.

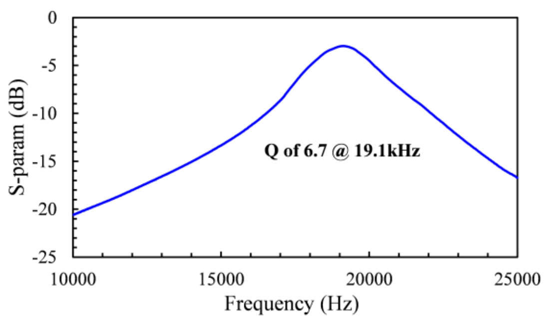

Figure 9: Near critically damped resonant characteristics (Q~6.7 @ 19.1kHz) of proof mass provides wide operational bandwidth.

In order to characterize performance of the accelerometer, a differential pair of two resonators is driven into resonance simultaneously using two independent phase-locked loops (PLL) with discrete TIAs implemented utilizing Zurich Instrument's lock-in amplifier (HF2 LI). The scale factor measurement was done by applying up to ±1g acceleration with 0.2g steps at 10Hz rate using a shaker table. The differential readout (Δf) is calculated with tracked resonant frequencies and the bias is nulled by subtracting the zero-g bias from the beat frequency. The differential readout shows 41.2Hz/g of scale factor (Fig. 10).

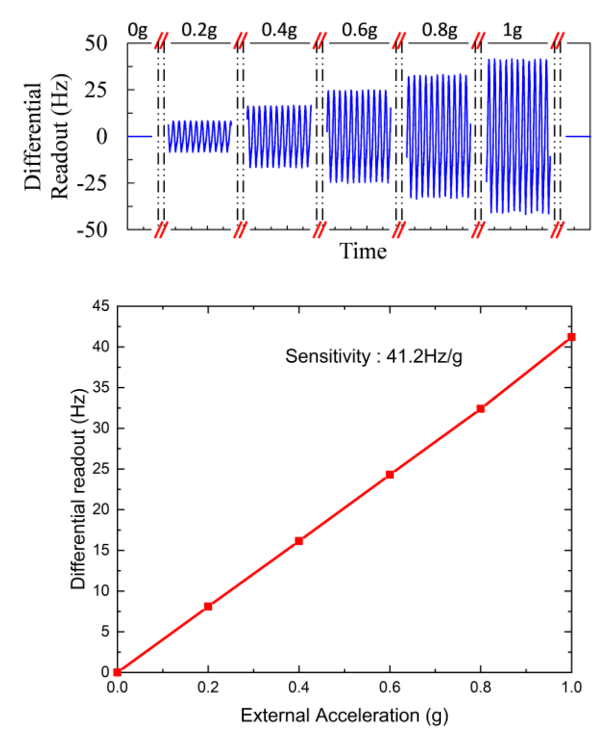

Figure 10: Shaker table measurement shows scale factor of 41.2Hz/g.

The Allan deviation plot of the accelerometer shows a measured velocity random walk corresponding to a noise density of 5.8µg/√Hz and a bias instability of 23µg (Fig. 11). The accelerometer shows excellent noise performance while showing relatively high bias instability starting to increase at short integration time of 0.1s. This is partially due to residual temperature effect of the resonators and partially due to the bias voltage stability. Better frequency stability is expected with proper temperature compensation techniques and more stable DC bias voltage source.

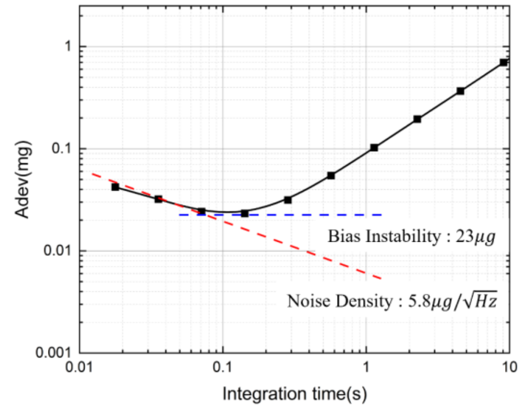

Figure 11: Measured Allan deviation of a prototype eFM OPA.

CONCLUSION

In this paper, the design and implementation of hermetically sealed differential readout out-of-plane eFM accelerometer have been presented and demonstrated its performance. Preliminary results show scale factor of 41.2Hz/g with over 15kHz of near critically damped, Q of 6.7, operational bandwidth. Alan variance analysis shows noise density of 5.8µg/√Hz and BI of 23µg, yielding superior noise and bandwidth performance required for high-end applications. Better frequency stability and measurability is expected with proper temperature compensation techniques.

REFERENCES

[1] Gupta, P., Moghimi, M. J., Jeong, Y., Gupta, D., Inan, O. T., & Ayazi, F. (2020). Precision wearable accelerometer contact microphones for longitudinal monitoring of mechano-acoustic cardiopulmonary signals. NPJ digital medicine, 3(1).

[2] Shin, S., Kwon, H.K., Vukasin, G.D., Kenny, T.W. and Ayazi, F., 2021. A temperature compensated biaxial eFM accelerometer in Epi-seal process. Sensors and Actuators A: Physical, 330, p.112860.

[3] Wang, J., Shang, Y., Chen, J., Sun, Z. and Chen, D., 2012. Micro-machined resonant out-of-plane accelerometer with a differential structure fabricated by silicon-on-insulator–MEMS technology. Micro & Nano Letters, 7(12), pp.1230-1233.

[4] Y. Jeong, A. Daruwalla, H. Wen, and F. Ayazi, "An out-ofplane "hinge-shaped" nano-gap accelerometer with high sensitivity and wide bandwidth," in 2017 19th International Conference on Solid-State Sensors, Actuators and Microsystems (TRANSDUCERS), 2017, pp. 2131-2134.

[5] Daruwalla, A., Wen, H., Gong, M. and Ayazi, F., 2020. High-G and High-Bandwidth Bulk Acoustic Wave (BAW) Accelerometers Using a Metal-Less AlN-HARPSS Process With 95 nm Gaps. IEEE Sensors Letters, 4(8), pp.1-4.

[6] Caspani, A., Comi, C., Corigliano, A., Langfelder, G., Zega, V., & Zerbini, S. (2014). A differential resonant micro accelerometer for out-of-plane measurements. *Procedia Engineering*, 87, 640-643.

[7] Wen, H., Daruwalla, A., Jeong, Y., Gupta, P., Choi, J., Liu, C.S. and Ayazi, F., 2018, April. Wafer-level-packaged HARPSS+ MEMS platform: Integration of robust timing and inertial measurement units (TIMU) on a single chip. In 2018 IEEE/ION position, location and navigation symposium (PLANS) (pp. 261-266).

CONTACT

*S. Shin; sshin312@gatech.edu